Exploring the repairing capabilities of high-performance glass fiber reinforced vitrimer composites

Lorenz, Niklas; Simonetto, Mirko; Wisniewsk, Valea; Riecken, Björn; Kumru, Baris

DOI
10.1016/j.compositesb.2025.113314

Publication date
2026

Document Version
Final published version

Published in
Composites Part B: Engineering

Citation (APA)
Lorenz, N., Simonetto, M., Wisniewsk, V., Riecken, B., & Kumru, B. (2026). Exploring the repairing capabilities of high-performance glass fiber reinforced vitrimer composites. *Composites Part B: Engineering*, *312*, Article 113314. https://doi.org/10.1016/j.compositesb.2025.113314

Composites Part B 312 (2026) 113314

Contents lists available at ScienceDirect

Composites Part B

journal homepage: www.elsevier.com/locate/compositesb

Exploring the repairing capabilities of high-performance glass fiber reinforced vitrimer composites

Niklas Lorenz [a,*,1], Mirko Simonetto [a,1], Valea Wisniewsk [b], Björn Riecken [b], Baris Kumru [a]

[a] Aerospace Structures & Materials Department, Faculty of Aerospace Engineering, Delft University of Technology, 2629 HS, Delft, the Netherlands
[b] CompriseTec GmbH, Rödingsmarkt 20, 20459, Hamburg, Germany

ARTICLE INFO

Keywords:
Vitrimer
Disulfide
Self-healing
Glass fibres
Composite repairing
Polymer-matrix composites (PMCs)

ABSTRACT

Vitrimers represent a class of polymers featuring dynamic covalent crosslinks that can undergo dynamic network rearrangements and hold a notable promise as recyclable thermosets with crack-healing capabilities. In particular, vitrimers with aromatic disulfide hardeners have emerged over the past few years. In these high-glass-transition polymers, the healing regime coincides with the onset of thermal degradation, posing a fundamental challenge for reconciling adequate network mobility with thermal degradation prevention. Therefore, the present study explores the repair capabilities of glass fiber-reinforced polymers (GFRP) with a vitrimer matrix to understand how the interplay of temperature, time, and pressure affects the repair.

A transferable framework for estimating a favourable time-temperature regime for vitrimer healing is introduced, based on thermal degradation and dynamic bond-exchange kinetics. The suggested optimized conditions are applied to repair different GFRP samples subjected to quasistatic intralaminar crack opening, and the extent of apparent mechanical property recovery is used to assess the repair effectiveness. Pressurized reconsolidation is required to restore the microstructure and repair cracks. When applying the prescribed repair conditions to the specific damage in short-beam samples, remarkable stiffness and strength recovery ratios of 93 % and 80 %, respectively, are achieved. Conversely, deviations from the prescribed regime due to improper dwell temperatures and times considerably reduce the recovery ratios of mechanical properties, limiting them to their residual values. However, the double cantilever beam repair conducted within the favourable regime shows that repair effectiveness depends strongly on the fracture surface morphology, revealing inherent limitations in the repair capabilities of the investigated laminate system.

1. Introduction

Epoxy resins are widely used matrix systems for fiber-reinforced polymers (FRPs) due to their exceptional dimensional and thermal stability, high mechanical performance, creep resistance, electrical insulation, and chemical resistance, making them indispensable in sectors such as aerospace and automotive engineering [1–4]. However, once cured, the three-dimensional covalent network of conventional epoxy thermosets renders them irreparable, insoluble, and non-recyclable, leading to significant end-of-life waste and limiting their sustainability compared to thermoplastics [5–8]. During service, these materials experience mechanical, thermal, and environmental loadings, which can cause long-term performance degradation [9–12], limiting their service life. Specifically, crack-like features, such as interlaminar delaminations, are common integrity-deterioration phenomena driven by cyclic loading [12] or impact scenarios [13], leading to irreversible fracture opening between the composite layers.

To overcome the inherent irreversibility of thermosets, dynamic covalent chemistries, including transesterification [14], disulfide [15–19], imine [20–22], siloxane [23,24], and urethane exchange [25] have been integrated into thermoset networks. This has led to the emergence of vitrimers, a class of covalently crosslinked polymers capable of macroscopic network rearrangements. These novel materials combine the mechanical and thermal robustness of thermosets with attributes previously exclusively reserved for thermoplastics, such as reprocessability, recyclability, and intrinsic self-healing [3,26–28].

* Corresponding author.
E-mail address: n.lorenz@tudelft.nl (N. Lorenz).
[1] Authors contributed equally.

https://doi.org/10.1016/j.compositesb.2025.113314
Received 7 November 2025; Received in revised form 3 December 2025; Accepted 11 December 2025
Available online 12 December 2025

Collectively, these features position vitrimers as a promising candidate to surpass conventional epoxy resins by enhancing service life by healing interlaminar delaminations during maintenance and reducing waste in structural applications [29].

Vitrimers heal through associative reversible bond-exchanges, enabling damage closure and interfacial restoration without the need for external healing agents. In contrast to extrinsic approaches based on microcapsules or vascular networks, which may introduce stress concentrators and reduce mechanical performance [30,31], vitrimer healing is intrinsic to the polymer architecture itself [32]. Numerous studies have explored vitrimer healing both at the resin level and within composite structures using different exchange mechanisms such as transesterification [33–39], siloxane [40] and imine exchange [41], and disulfide metathesis [31,42]. Across these systems, healing is typically activated by heating the material above its glass transition temperature (T_g) while applying moderate pressure. Reported repair cycles vary widely (e.g., 150–200 °C, 0.2–10 MPa, with dwelling times of minutes to hours) and can effectively restore properties such as tensile strength, stiffness, interlaminar shear strength (ILSS), and fracture toughness, with repair efficiencies exceeding 85 % [33–42]. However, the number of attainable repair cycles strongly depends on underlying chemistry, with some systems showing a decline in healing efficiency after repeated activation due to thermal aging, oxidation, or volatile release [34,36–38]. These observations highlight the delicate balance between the network mobility required for macroscopic rearrangements and the maintenance of matrix durability.

Despite the promising healing performance reported in the literature, the majority of vitrimer matrices investigated for FRPs exhibit T_g values below 120 °C, which restricts their use in high-temperature aerospace environments. For structural applications, the matrix typically requires $T_g \geq 180$ °C, since the design limit is often defined by lowering the measured T_g by a prescribed margin of 28 °C (50 °F) to ensure long-term thermal stability [43]. A major limitation is that triggering bond exchange (and associated repairability) requires operations above T_g, which, for high-performance systems, demands extreme temperatures (>200 °C). At such temperatures, thermal degradation and detrimental side reactions narrow the processing windows, and reduced healing efficiency becomes a critical concern [31,37,38,42].

Nevertheless, some recent advances include transesterification-based matrices with T_g of at least 174 °C [37,38] and disulfide-based systems with T_g up to 233 °C [18,31,42,44,45], although booth reveal inherent limitations under prolonged and repeated high-temperature exposure. Hand-laminated CFRP with vitrimer matrix (aromatic thermosetting co-polyester (ATSP) with $T_g = 174$ °C [37]) show 50 % recovery of stiffness and strength values after healing at 280 °C for 2 h (0.03 MPa). By focusing on the fracture toughness, K_{IC}, initial repairing efficiencies of 100 % decreased to less than 20 %, independent of the temperature program, after four repeated repairing cycles, which is attributed to thermal degradation and formation of volatile species along the crack surfaces [38]. For the ATSP systems, the selected repair protocol itself critically determines the archievable repair efficiency.

Besides ATSP, vitrimer matrix systems relying on disulfide exchange seem a promising candidate for structural applications, as basic chemicals such as aromatic disulfides (4-aminophenyl disulfide, 4-AFD) are already available on a kilogram scale and do not require individual synthesis. Beyond this, several studies have already verified their processability across different established composite processes [28,42,46–48]. The effect of repairing (10 min at 200 °C, 10 MPa) of GFRP with disulfide vitrimer matrix ($T_g = 174$ °C [31]) on $G_{II,c}$ and ILLS is investigated in Ref. [31]. To reach sufficient repairing efficiency and accelerate repairing, it required to adjust the amine to epoxy stoichiometries from 1 to 1.2 (but at the same time decreasing T_g) yielding initial repairing efficiencies of 89 % and 60 % for the $G_{II,c}$ and ILLS values, but decaying to efficiencies of 50 % and 25 % after ten repairing cycles. An aero-grade epoxy resin (T_g of 175 °C [7]) is used to manufacture CFRP in RTM [45]. In addition to a negligible knockdown effect compared to the established RTM 6 benchmark resin, the authors demonstrate that 2 h of healing at 220 °C with 2 MPa applied pressure yields ILLS repair efficiencies of 72 %. The reduced healing efficiency is attributed to micro delaminations and cracks that are difficult to repair [45]. As shown in Ref. [49], the thermal stability of these resin systems appears to be primarily governed by the thermal stability of the disulfide bonds within the hardener, therefore constituting a key constraint when the material is subjected to prolonged exposure at elevated temperatures. Even higher T_g of 233 °C are demonstrated by utilizing RTM 6 monomer and aromatic 4-AFD hardener. CFRP laminates manufactured in resin transfer molding exhibit promising mechanical properties [42]. Applying compressive pressure of 4 MPa (at 245 °C for 15 min) to the CFRP has been found insufficient to close matrix cracks oriented at 45° to the lamination plane, although delamination can be effectively repaired. In addition, the narrow reprocessing window and modest dynamic bond-exchange rates of the vitrimer at the reprocessing temperature constrain the repair efficiency, which remains in the range of 12–23 % [42].

While these studies confirm the potential of high-T_g vitrimers, they concurrently reveal practical limitations such as incomplete crack closure, restricted reprocessing windows, viscosity-driven manufacturing defects, and rapid decline in healing efficiency with repeated repair cycles at elevated temperatures [31,38,42,44]. Overall, the literature highlights the need to preserve the effectiveness of healing during thermal treatment by balancing adequate network mobility with the prevention of thermal degradation. These limitations in current vitrimer systems, particularly the narrow processing windows, susceptibility to thermal degradation, and the scarcity of high-T_g matrices capable of efficient repair reveal a critical knowledge gap in understanding how temperature, time, and pressure collectively govern repair efficiency. Understanding this entangled relationship between repair conditions and degradation behaviour is essential to establishing controlled, certifiable repair procedures suitable for aerospace-grade composite structures. The overarching objective of repair in such systems is to restore mechanical performance after matrix-dominated damage, thereby extending service life, reducing maintenance needs, and decreasing environmental impact through improved durability and reduced component replacement.

In previous work, the authors developed a high-performance disulfide-based vitrimer system with a T_g of 195 °C. The resin system, formulated from an industrial-grade resin, demonstrated processing characteristics comparable to those of the widely used RTM6. Incorporating a biobased reactive diluent increased network flexibility, accelerated dynamic bond exchange kinetics, and expanded the temperature range over which healing can be performed [18]. This material offers a rare combination of aerospace-relevant thermal stability, low viscosity for liquid composite molding, and accelerated dynamic covalent adaptability, making it a promising candidate for high-temperature self-healing composites.

Building upon this foundation, the present study provides a static evaluation of the repairability of this high-T_g vitrimer system, aiming to:

- Characterize the **matrix-level healing and thermal degradation** phenomena, thereby identifying the operational limits given by the time-temperature regime required for effective healing.
- Introduce a **framework to derive temperature–time–pressure profiles** that enable an effective one-time repair of specific damage modes in composite laminates, while minimizing degradation.
- Evaluate the **repair efficiency of fiber-reinforced laminates** by computing the recovery ratio of relevant apparent material properties. Specimens are loaded to fracture using standardized mechanical testing that promotes crack opening, and repair protocols derived from the matrix characterization are applied.

Therefore, this work represents a systematic investigation of the repairability of aerospace-grade, high-T_g disulfide-based vitrimer composites. Through an integrated approach combining degradation-kinetic modeling, viscoelastic characterization, and experimental validation of composite-scale repair performance, the findings provide a foundation for designing appropriate repair protocols that balance repair performance and degradation, ultimately supporting the development of certifiable repair strategies for vitrimer-based structural composites.

2. Materials and methods

2.1. Materials

The epoxy monomer of the two-component aero-grade qualified epoxy resin EPIKOTE™ 600 provided by Westlake Corp., US, serves as the basis for the vitrimer resin formulation. Similar well-established aero-grade resin systems, such as RTM 6 by Hexcel Corporation and Cytec 890 RTM by Syensqo S.A., rely on identical aniline platforms, suggesting that the results provided in the present work might be relevant for a broader range of resin systems. 4-aminophenyl disulfide (4-AFD), purchased from Molekula Ltd, UK, crosslinks the system and introduces dynamic S–S bonds into the network. Besides that, multifunctional biobased cardanol-derived reactive diluent LITE 513DF from Cardolite Corp., US, increases the flexibility of the network, supports fast stress relaxation, and prevents excessively high glass transition temperatures and overlapping of the temperatures required for dynamic bond exchange ($T > T_g$) with the degradation range of the material [18]. The overall amine/epoxy hydrogen equivalent ratio was kept at 1.28 to accelerate bond exchange. The exact stoichiometry can be taken from Ref. [18]. Additionally, extensive characterization of the resin has been previously carried out, and basic mechanical and physical properties are provided in Ref. [18].

Neat resin films and rods for dynamic mechanical analysis (DMA) and small dog-bone bars (DIN EN ISO 527-2, Type A22) were cast in a two-sided metal mold applying the protocol described in Ref. [18].

Glass fiber fabrics (220 g/m^2 Interglas 92145 by Porcher Industries S. A., France) were used to manufacture a composite with aircraft-grade glass fibers. This quasi-unidirectional (UD) plain weave textile contains a high warp content of five 68 tex EC9 glass rovings (monofilament diameter 9 μm) for every 22 tex EC7 glass roving (monofilament diameter 7 μm) used as weft. All fibers are sized with a silane-based sizing combined with Chromium(III)-methacrylate (type FK 144) to promote adhesion to the matrix material. The manufacturing of FRP laminates is described in the supplementary material and consists of two process steps: First, the quasi-UD glass fiber fabrics were pre-impregnated utilizing the roller impregnation process DirectPreg® (Fig. S1a). This technology enables prepreg production with limited material quantities while maintaining precise control over fiber and matrix content. Pre-impregnated layers were stored in frozen conditions. Second, the pre-impregnated sheets were stacked in two distinct sequences of 12 and 24 layers (Table S1), respectively, and press-consolidated, with average thicknesses after consolidation of 1.8 mm (laminate I) and 3.8 mm (laminate II). Consolidation of the prepregs was carried out in a heated press (KV 217.00 1000 kN, RUCKS Maschinenbau GmbH, Germany) with a tailored temperature profile ranging from 80 to 160 °C (Fig. S1b), while applying a pressure of 1 MPa to minimize bleeding of the fabric, resulting in an average fibre volume content in the fibre direction of 56.5 vol%. The choice of glass fibers rather than a more performant reinforcement material was driven by the research question of this work, which focuses on understanding fracture phenomena governed by the matrix. The relatively lower stiffness of glass fibers enables greater deformation and load transfer to the matrix, thereby increasing sensitivity to the analyzed damage modes and their subsequent repairs.

Laminate I (cf. Fig. S1c) was cut to short beam samples (8 × 25 mm^2), while laminate II was cut to double cantilever beam (DCB) samples (24 × 250 mm^2). The stacking sequences (Table S1) were selected to enable a robust manufacturing process (minimizing in-plane layer movement during pressurized consolidation) while ensuring significant stiffness in the beam direction, as required for the two selected laminate testing methods. The cut operation is performed using a diamond disc. All samples are subsequently conditioned at 170 °C for 30 min to ensure reproducible conditions by fully curing the matrix material and stabilizing moisture levels.

2.2. Experimental methods

In this section, the applied resin and laminate testing methods, as well as the laminate repair process, are detailed. First, the neat resin degradation and bond exchange kinetics are characterized, providing a basis for identifying a suitable resin-healing regime. After this, the impact of thermogravimetric degradation is assessed by examining the deterioration of mechanical properties for both the resin and the laminate, thereby constraining the processing window for laminate repair. Further, repair capabilities are assessed by retesting specimens intentionally loaded to failure and then subjected to the designated repair process.

2.2.1. Characterization of resin materials

Thermogravimetric analysis (TGA) was carried out using a TGA 4000 from PerkinElmer, Inc., US. All measurements were performed in air at a constant flow rate of 20 mL/min. Samples with masses ranging from 15 to 25 mg were heated from 25 to 900 °C at heating rates of 5, 10, 15, and 20 K/min, and the mass loss was recorded.

DMA testing was performed to quantify the effect of 20 min of elevated temperature dwellings (180, 200, 215, 220, 240 °C), resulting in different small degradation states, on the relaxation times (i) and T_g (ii) of the neat resin, tensile stress relaxation trials, and oscillating temperature ramps in the bending fixture are carried out with an RSA-G2 device from TA Instruments, US. For (i), films (6 × 0.9 × 40 mm^3) were submitted to an instantaneous stress of 1 % at 220 °C. After first allowing temperature equalization for 5 min, the decay in stress was recorded for 10^3 s. For (ii), rectangular specimens (9 × 2 × 25 mm^3) were heated in air at 3 K/min from 30 to 250 °C. Measurements were performed with automatic force tracking at 1 Hz while applying a dynamic displacement of 10 μm (in the linear viscoelastic regime).

Additionally, short tensile specimens were subsequently subjected to 20 min dwellings at elevated temperatures (180, 200, 215, and 240 °C) in a convection oven (Vötsch VTL, Vötsch GmbH, Germany) to assess the influence of thermal material degradation on quasistatic performance. Tensile tests were conducted at a strain rate of 0.25 mm/min using a Universal Testing Machine Z10 (ZwickRoell AG, Germany). A total of 5 specimens were tested for each degradation state, and an extensometer with a 15 mm gauge length was mounted on each specimen to record displacement.

2.2.2. Characterization of the laminate repairability

Laminates are tested in the form of short beams and DCB specimens to understand the two distinct, superimposed phenomena analyzed in this work: First, the effect of thermally induced matrix degradation due to isothermal dwellings is analyzed on intact short-beam laminate samples. Second, the matrix healing capability is evaluated by loading the laminate samples to fracture and assessing the recovery of relevant mechanical properties after the repair. The repair process concept consists of keeping the crack surfaces closed at a prescribed temperature for a defined time. Under ideal conditions, the cracked interface would be fully restored, and the sample would require the same amount of energy to reopen as before fracture.

Short-beam samples degraded selectively are tested for their dynamic mechanical response using DMA, as with the neat resin samples. Equivalent isothermal holding times and temperatures as for the neat resin characterisation are applied to permit a comparison between

laminate and neat resin behaviour. The short-beam samples were heated under air at 3 K/min from 30 to 230 °C. Measurements were performed in the single cantilever bending mode at 1 Hz, with a dynamic displacement of 0.1 %.

The short-beam testing method defined by the standard D2344/D2344M − 22 [50] was selected to selectively promote a fracture phenomenon whose initiation is mainly controlled by the matrix shear. The Universal Testing Machine Z10 (ZwickRoell AG, Germany) was set up with a short bending fixture with a support span of 13 mm and a punch diameter of 10 mm. The crosshead displacement-controlled speed was set to 0.5 mm/min, and data collection was initiated after a defined preload of 0.1 kN was reached. Virgin short beam samples are loaded until the first load drop caused by fracture opening. After unloading, a reduced loading ramp was applied to determine the apparent residual stiffness after the initial failure. To observe the failure mechanism, images of damaged cross-sections are captured using a confocal optical microscope (VK-X1000 from Keyence Corp., Japan) at 20x magnification. The fracture surface is scanned using a structured-light optical microscope (VR 5000 from Keyence Corp., Japan) at 12x magnification.

Following the methodology applied to the short-beam specimens, double-cantilever beam static testing and the associated fracture-toughness evaluation are performed using the same testing machine with an adapted setup. This analysis is conducted to examine the repair capability of a crack that is nominally similar in appearance but initiated and propagated under a different loading mode, primarily tensile. Therefore, two DCB samples are tested following the ASTM D5528-21 methodology [51] at a constant displacement-opening rate of 4 mm/min, with the crack tip position recorded via timed camera acquisitions. To perform this test, two aluminium blocks (with surface area of 24 × 20 mm^2) are adhesively attached to the beam's open extremity with cyanoacrylate adhesive to allow the application of the opening load, and a precrack is initiated by sliding a razor blade between the non-adhered beam interfaces. The initial delamination precrack length for both pristine samples was 60 mm from the load application point. After testing, the aluminum blocks are removed to enable the sample repair process.

A preliminary evaluation of the repair process is performed using both oven conditioning of vacuum-bagged samples and press heating to determine the applicable methods for this system. The hot-press used was a Joos LAP100 (Gottfried Joos Maschinenfabrik GmbH, Germany) hydraulic machine with a heated plate size of 600 × 600 mm^2 and a maximum load of 1000 kN. Specimen surface area is measured before repair to ensure uniform pressure application across different samples. Due to the relatively small short beam sample size compared with the available press specifications, the repair pressure is set to the minimum applicable stable force, using the available control system. Accordingly, a repair pressure of 10 MPa was selected. Both short-beam and DCB samples have been repaired individually at the selected pressure, with different time and temperature dwellings determined by the preliminary evaluation of the matrix vitrimeric material presented in the results section. During the DCB sample repair, a non-adhesive PTFE film is interfaced between the original non-adherent region.

2.3. Analytical methods

Different analytical methods are used to define the process window for repair, which is limited by the kinetics of vitrimer degradation at elevated temperatures and by simultaneously occurring bond exchange. Additionally, the stiffness and strength recovery rates are evaluated to gain insight into laminate healing capacities.

2.3.1. Kinetic modelling of degradation

Kinetik modelling of degradation represents an important step to correlate arbitrary temperature histories of the material with the resulting degradation. Therefore, the recorded mass loss during TGA for multiple heating rates is utilized to model the degradation of vitrimer matrix based on model-free kinetics [52,53]. TGA registers a mass change of the sample over time and temperature during heating in air. The actual weight $m(t)$ is then converted into conversion $\alpha(t)$, representing the apparent degradation:

$$\alpha(t) = \frac{m_0 - m(t)}{m_\infty - m_0}, \tag{1}$$

while m_0 and m_∞ represent the initial and final mass of the sample. By introducing a generalized kinetic equation, the gradation rate $\frac{d\alpha}{dt}$ may be described by a temperature-dependent rate constant $k(T)$ and a mass-dependent reaction model $f(\alpha)$ [54]:

$$\frac{d\alpha}{dt} = k(T) f(\alpha). \tag{2}$$

While assuming that $k(T)$ follows Arrhenius law and applying a constant heating rate β, the degradation rate $\frac{d\alpha}{dt}$ can be numerically calculated from the temperature and conversion data according to:

$$\beta \frac{d\alpha}{dT} = \exp\left(\frac{-E}{RT}\right) f(\alpha), \tag{3}$$

where $\beta = \frac{dT}{dt}$, represents the heating rate, E the apparent activation energy of the degradation process, and R the universal gas constant. The mathematical manipulations of Equation (3) enable the determination of kinetic triples (E, A and $f(\alpha)$) utilizing the degradation data obtained from the TGA measurements at multiple heating rates.

Multiple methods (analytical and computational) have been proposed to approximate data derived from dynamic TGA measurements into an appropriate mathematical expression. In this context, isoconversional methods provide meaningful insights into mechanistic analysis, detecting governing degradation mechanisms [55,56]. The isoconversional principle states that the degradation rate $\frac{d\alpha}{dt}$ at a certain isoconversional value ξ ($0 \leq \alpha \leq 1$) is solely a function of temperature [57,58]:

$$\left[\frac{\partial \ln\left(\frac{d\alpha}{dt}\right)}{\partial T^{-1}}\right]_\alpha = -\frac{E_\xi}{R}, \tag{4}$$

whereas E_α is the apparent activation energy for a conversion α, and R is the universal gas constant. Based on Equation (5) a model-free value of the apparent activation energy can be estimated for each α value. Within the present work, we utilize the differential Freedman's method [59]:

$$\ln\left(\frac{d\alpha}{dt}\right)_{\alpha,i} = ln[A_\alpha f(\alpha)] - \frac{E_\alpha}{RT_{\alpha,i}}. \tag{5}$$

Applying this method requires knowledge of the degradation rate $\left(\frac{d\alpha}{dt}\right)_{\alpha,i}$ and the corresponding temperature $T_{\alpha,i}$ for a specific extent of conversion α across i temperature programs utilized [55]. The E_α values are calculated for α ranging from j = 0.02–0.20 within steps of 0.001 yielding N = 180 discrete steps, considering values above 0.2 not of practical relevance for degradation during the processing.

The four temperature programs include heating with constant heating rates β_i of 5, 10, 15, 20 K/min which represent heating rates occurring during repairing of vitrimers. For each β_i, the $\left(\frac{d\alpha}{dt}\right)_{\alpha,i}$ and $T_{\alpha,i}$ values are determined. As the term $ln[A_\alpha f(\alpha)]$ remains constant for a particular value of α, the left-hand side of Equation (5) depends linearly on the reciprocal temperature. Taking advantage of this linear correlation, the effective E_α can be calculated from the slope while $A_\alpha f(\alpha)$ represents the y-intercept, respectively.

To solve this problem for an arbitrary temperature program T(t), the approach suggested *by Farjas and Roura* can be applied [60] to discretize the dependence of temperature on time into constant time intervals, Δt,

so that $t_k = k\,\Delta t$ where k is a natural number and $T_k = T(t_k)$. The method is derived directly from Eq. (2) by replacing the differentials by increments yielding:

$$\alpha_{k+1} = \alpha_k + A_{\alpha,k} f(\alpha_k) \exp\left(\frac{-E_{\alpha,k}}{RT_k}\right) \Delta t. \tag{6}$$

Distinct pairs of activation energy and pre-exponential factors with defined Δt of 0.1 s. $E_{\alpha,k}$ and $A_{\alpha,k} f(\alpha_k)$ in Equation (6) are interpolated from discrete sets of $E_{\alpha,j}$ and $A_{\alpha,j} f(\alpha_j)$ [52] with j values defined above. Following the methodology outlined, kinetic evolutions through direct time integration of the transformation rates are employed to predict the kinetics of decomposition under arbitrary temperature profiles.

2.3.2. Modelling of stress relaxation

Stress relaxation in the rubbery state is commonly utilized to access the bond-exchange kinetics and to gain insight into the temporal order of magnitude of healing capacities. The Kohlrausch–Williams–Watts (KWW) stretched exponential decay [61] is selected to fit the tensile stress relaxation response for the different degradation states:

$$\frac{E(t)}{E_0} = exp\left[-\left(\frac{t}{\tau^*}\right)^{\beta}\right], \tag{7}$$

where τ^* represents the relaxation time, β the stretching exponent, and $E(t)$ the decay in relaxation modulus at time t related to its initial value E_0. The β values ($0 < \beta \leq 1$) describe the width of the relaxation time distribution, with lower β values associated with greater width and more heterogeneous segmental dynamics [62]. The parameters β and τ^* are fitted for each temperature and subsequently the average relaxation time is calculated as follows [63]:

$$\langle \tau \rangle = \frac{\tau^* \Gamma\left(\frac{1}{\beta}\right)}{\beta}, \tag{8}$$

where Γ is the gamma function. Still, in the present case, as relaxation trials are conducted close to the α-transition regime, relaxation may be affected by the glassy dynamics, and disulfide metathesis may not be the only rate-limiting process. Therefore, we introduce a weighted KWW function with double exponential decay:

$$\frac{E(t)}{E_0} = w \cdot exp\left[-\left(\frac{t}{\tau_g^*}\right)^{\beta_g}\right] + (1-w) \cdot exp\left[-\left(\frac{t}{\tau_d^*}\right)^{\beta_d}\right], \tag{9}$$

with w representing the weight factors and τ_i^* the β_i the individual contributions for the short mode glassy (g) and long mode dynamic bond exchange dynamics (d).

2.3.3. Evaluation of laminate properties changes and repairing recovery rate definitions

As discussed in the experimental methods section, short-beam and DCB samples are tested after different preconditioning and repair processes. In this section, the relevant changes in properties are introduced, and the recovery rates are defined accordingly. Short beam samples are processed according to the standard D2344/D2344M − 22 evaluations [50], but with a focus on accounting for apparent material property changes associated with microstructural damage formation, as shown in Fig. 1 and discussed in this section. For each of the samples, load and crosshead displacement data is recorded. The stiffness K computed during the elastic regime is the slope of the applied load versus crosshead displacement. It is referred to as the apparent stiffness, as it is not a material property but the result of the machine structure and test setup.

Still, for the evaluations and discussions relevant to this paper, the apparent stiffness recorded during the short-beam test is highly valuable for demonstrating changes in material integrity. To understand the extent of the damage after the first failure event, the residual stiffness

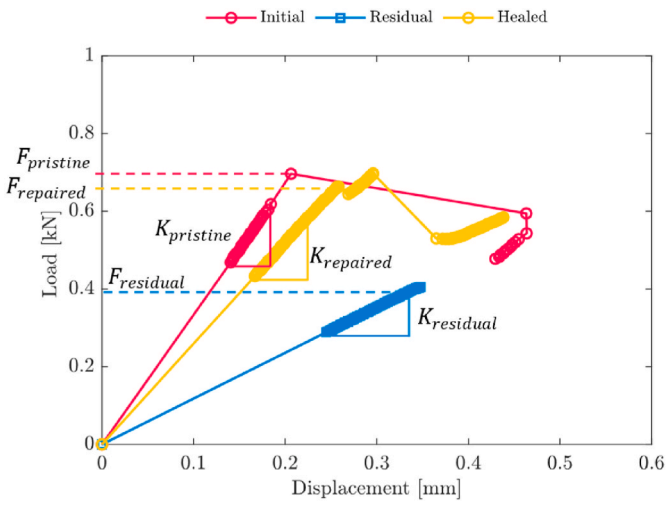

Fig. 1. Representation of the load ramps for a single short-beam sample tested. The load ramps for initial failure, residual stiffness, and repaired evaluation are represented together with the key characterized apparent properties.

$R_{SB,Stiffness}$ recorded during specimen unloading and during an additional loading ramp performed in the elastic region to determine the change in behaviour after the formation of damage features.

$$R_{SB,Stiffness} = \frac{K_{failed}}{K_{virgin}}. \tag{10}$$

In fact, after interlaminar shear damage, the specimens exhibit lower compliance due to the opening of interlayer cracks and sliding at opposing interfaces. After the repairing process, each sample is tested again to failure, and the repairing efficiency $\eta_{SB,stiffness}$ in terms of apparent stiffness is computed by relating the repaired apparent stiffness to that of the undamaged sample:

$$\eta_{SB,stiffness} = \frac{K_{repaired}}{K_{virgin}}. \tag{11}$$

Note that this should not be considered an absolute value, as the starting point is the residual stiffness rather than a fully damaged sample. The measurement of the strength is achieved in both cases at the peak load F just before a load drop, resulting in a change in the load displacement ratio. The short beam strength S is calculated for each sample considering the sample size and a factor of 0.75 as defined in the standard. When computing the ratio of recovered strength, this information is annulled. In fact, the strength recovery ratio is defined as:

$$\eta_{SB,strength} = \frac{S_{repaired}}{S_{virgin}} = \frac{F_{repaired}}{F_{virgin}}. \tag{12}$$

Please note that recovered strength is a significant parameter when the stiffness recovery ratio is close to 1, as it reflects the strength of the healed interfaces. Instead, suppose the stiffness recovery ratio is close to the residual stiffness, almost no repair is registered. In that case, this parameter loses significance as it compares the strength of two different, subsequent failure modes.

DCB tests are processed according to ASTM D5528-21 standard [51]. Specifically, the compliance calibration method is employed to compute the applied strain energy during the test progress. The mode I fracture toughness recovery rate $\eta_{rep,DCB}$ is calculated in a similar fashion to Ref. [40], focusing on the average propagation toughness between the virgin and healed samples.

$$\eta_{rep,DCB} = \frac{G_{IC,repaired}}{G_{IC,virgin}}. \tag{13}$$

The computed toughness resulting from the static test progression is

reported along the propagated crack length for both the virgin and healed samples.

3. Results and discussion

This section discusses the results from the characterization of the matrix material and the consequent selection of the repairing process. Subsequently, the design of experiments is applied to evaluate the effect of processing conditions on the repairing efficiency.

3.1. Kinetic model for the thermogravimetric degradation

Normalized masses recorded different heating rates (Fig. S2a) provide the basis for the kinetic modelling of the degradation process. By applying Friedman's differential method, we obtain the activation energy and preexponential values for discrete points within the selected α range of 0–0.2 (Fig. 2a, Fig. S2b).

A comparison of measurements and model (Fig. S2c) reveals good agreement, with mean average errors ranging from 0.3 to 0.5 % across the different heating rates. This manuscript determines kinetic evolutions by directly integrating the transformation rates and may be employed to predict decomposition kinetics under isothermal and dynamic conditions, and to derive time-temperature-transformation diagrams for the thermal degradation of the vitrimer matrix (Fig. 2b). The diagram allows users to select temperature-time pairs to selectively adjust the degradation state and examine the resin's thermomechanical and mechanical responses.

3.1.1. Effect of degradation on glass transition temperature and bond exchange kinetics

Degradation modelling and relaxation times of the neat resin system set the boundaries for tailoring repairing cycles that minimize degradation while enabling sufficient time for dynamic bond exchange to heal the intentionally induced cracks in the FRP. Resulting degradations are calculated by solving (6) for the isothermal dwellings, yielding values of up to 2.5 % for the specimens subjected to 240 °C. The temperature-dependent modulus developments from oscillating temperature sweeps are shown in Fig. 3a, stating that the glass transition temperature T_g remains largely unaffected up to temperatures of 200 °C while the T_g decays to lower temperatures at more elevated dwelling temperatures. This circumstance could be explained by the decomposition of the disulfide cross-linkage, resulting in a reduced cross-linking density. Besides that, thermal degradation above 0.5 % reflects in lower tan δ peak values and a broader α transition. The observed decrease in the maximum tan δ is likely due to oxidation-induced stiffening of the network, which restricts overall molecular mobility and reduces viscoelastic dissipation. Interestingly, no explicit secondary peak is observed, as might be expected from the formation of an oxidized outer layer in the material [64,65]. Still, the peak broadens, especially at 2.5 % degradation, which may be attributed to a secondary peak arising from increased oxidative cross-link concentration in the material. Furthermore, the initial storage modulus decreases because temperatures above 75 °C may already initiate the α-relaxation, involving the local motion of flexible, long-chain aliphatic groups in the cardanol-based reactive diluent (and therefore decreasing the modulus), thereby triggering the many-molecule cooperative glass transition [18].

Besides the structural changes, the relaxation times at 215 °C are assessed for different degradation states. It is common practice to quantify bond exchange kinetics using isothermal tensile relaxation tests at elevated temperatures. Figure S3a and Figure S3b show the relaxation modulus, the normalized relaxation modulus, and the fit of the weighted Kohlrausch−Williams−Watts functions (Equation (9)) for different degradation states. The derived parameters from Equation (9) are provided in Table S2 and $\langle\tau_g\rangle$ and $\langle\tau_d\rangle$ are provided in Fig. 3b for different cure states. It should be noted that complete relaxation is not achieved even in the pristine state, and even with an excess of amine at an amine-to-epoxy ratio of ~1.3, which is reported to increase bond exchange rates [15,64], resulting in complete relaxation in Ref. [66]. One explanation could be that the relaxation is carried out close to the α-transition, so that bond exchange, to a certain extent, remains limited by the glassy regime. The $\langle\tau_d\rangle$ values decline with processing degradation, which indicates a faster dynamic bond exchange and may be attributed to a decreased crosslinking density by the degradation of the disulfide crosslinking points. The decreased relaxation modulus (Fig. S3a) is indicative of a lower crosslinking density. The disulfide hardener is expected to decompose first, as demonstrated by the detection of sulfur dioxide during TGA measurements [49]. Furthermore, the relative residual stress values increase (Fig. S3b), which can be attributed to the reduced number of dynamic disulfide bonds within the network.

Interestingly, thermogravimetric degradation, primarily driven by cleavage and oxidation of disulfide bonds, can temporarily accelerate relaxation behavior and associated dynamic bond exchange, thereby supporting the repair process. In the long term, however, the stress-relaxation capabilities due to a reduction in dynamic bond sites decrease, leading to the loss of the network's dynamic character, which is detrimental to the repair and malleability features of vitrimers resulting from macroscopic flow.

3.1.2. Effect of degradation on resin tensile properties

Stress-strain diagrams resulting from tensile testing of flat resin samples with different degradation states are shown in Fig. S4a. The computed stiffness, failure strain, and strength are provided in Fig. 3c

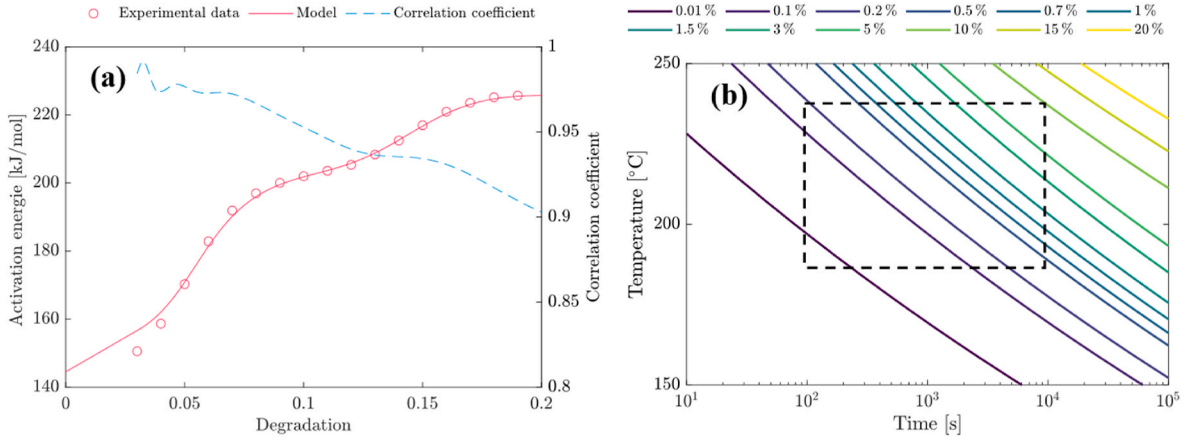

Fig. 2. Derived activation energies of degradation based on Friedman's model (a). Isoconversional lines for degradations of 0.1 %–20 % with relevant processing regimes indicated in the dashed square (b).

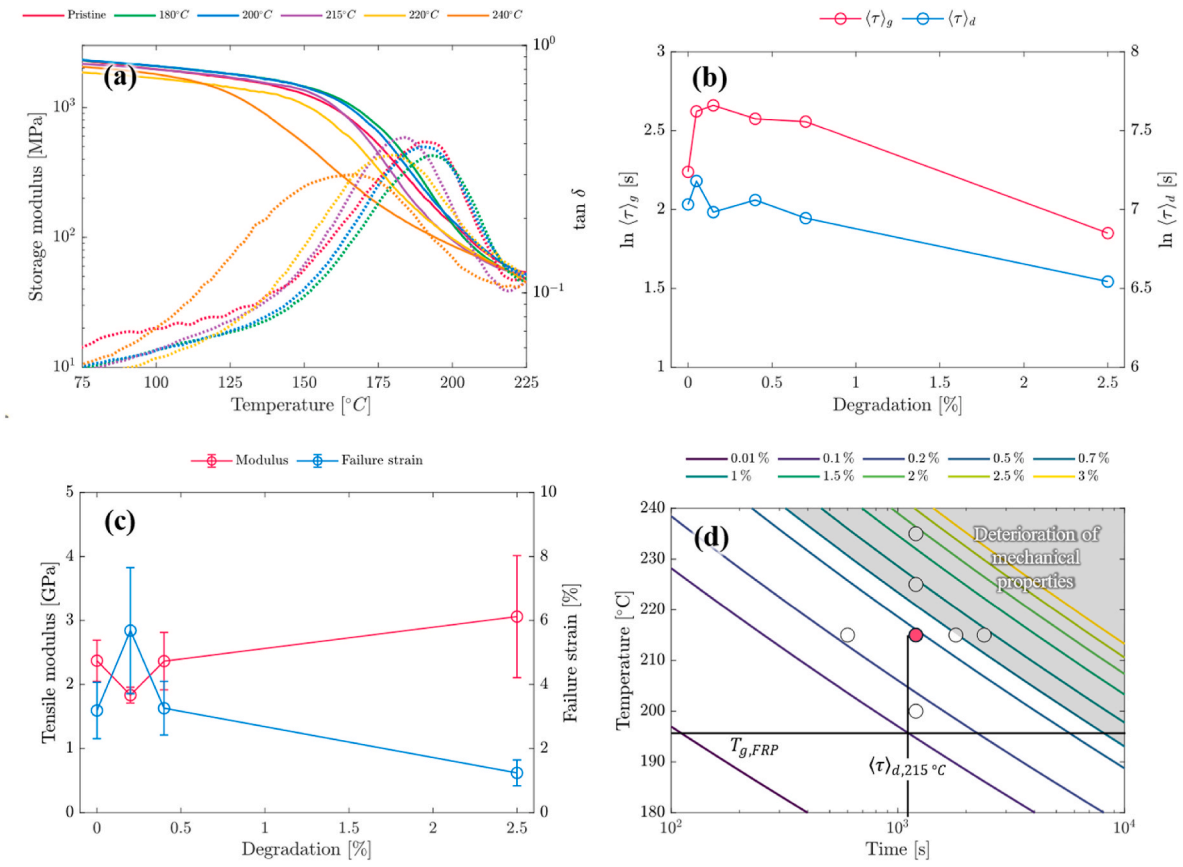

Fig. 3. Modulus development of the neat resin after isothermal dwellings for 20 min (a). Correlation of bond relaxation times at 215 °C and degradation state resulting from different isothermal dwellings (b). Tensile testing of different degradation states resulting from thermal histories (c). Time-temperature transformation diagram for the thermal degradation. Circles indicate experimental points, and red circles represent the central point for the design of the experiments (d).

and Figure S4b. Degradation values of 0.2 % resulting from dwelling at 200 °C increase the failure strain, which may be attributed to residual crosslinking caused by unreacted functional groups that are often trapped in the polymer network. As the modulus decreases with continued crosslinking [67–69], caused by a more limited chain mobility of the crosslinked molecular structure, evoking a reduced packing density. Consequently, a higher free volume is frozen in the glassy state, resulting in a drop in modulus at 0.2 %. Additionally, diffusion-limited oxidation in the resin forms an outer oxide layer, which may explain the continuous increase in sample stiffness observed in micro indentation testing [70]. However, with proceeding degradation, local heterogeneity and micro-void formation in the oxide layer can cause localized stress concentration, leading to earlier failure (embrittlement) [64], thereby reducing the tensile strength by 41 % (Fig. S4b) and decreasing the failure strains from 3.2 % to 1.2 % (Table S3). The surface-near oxidation shows a gradual color change with the conditioning parameter, as observed during microscopic investigation (Fig. S5). Therefore, from this observation, it can be hypothesized that in the base material, the increase in modulus due to oxidation is compensated by residual crosslinking up to a limit thermogravimetric degradation level of 0.5 %. However, thereafter, mechanical performance declines detrimentally.

3.1.3. Design of repairing cycles

A processing map is used to outline the repair conditions generated and is shown in Fig. 3d. Based on the results obtained from analyzing the resin's properties, a time-temperature superposition diagram is created to describe how the material thermally degrades over time. DMA and quasistatic testing revealed that once the resin experiences more than 0.5 % mass loss, its mechanical performance begins to deteriorate significantly, as evidenced by decreasing T_g and failure strain (cf. Fig. 3a and b). This establishes a strict upper limit for the time-temperature conditions of the healing process. Fig. 3d indicates that a mass loss of just below 0.5 % occurs at 215 °C (and thus approximately 20 °C above the T_g) after 22 min of isothermal dwellings. Processing temperature closer to the maximum T_g would impede the bond exchange due to the predominance of the glassy regime. Therefore, within the identified 22 min window, the processability can be deemed acceptable only if the healing process proceeds quickly enough to be completed within this designated time frame. In detail, enabling dynamic bond exchange, which is the reversible chemical reaction responsible for the healing process, still requires a minimum characteristic time $\langle\tau_d\rangle$. This time, which depends on temperature and the degree of resin degradation, is characterized by relaxation tests (as detailed in Fig. S3 and Table S2). At 215 °C, the dynamic bond relaxation time $\langle\tau_d\rangle$ of 19.4 min falls within the range of the designated time window of 22 min, setting the central point for repairing, simultaneously balancing healing capabilities and thermal degradation. The other repair parameters are then deliberately set towards critical levels to quantify the effects of deviations from the specified processing conditions. The identified processing time and

Table 1
Identified polymer healing conditions.

Index	Temperature [°C]	Time [min]
1	200	20
2	215	20
3	225	20
4	235	20
5	215	10
6	215	30
7	215	40

temperature parameters are summarized in Table 1, with the central identified point designated as index 2.

3.2. Evaluating the laminate

In this section, the experimental behavior of laminates under increased degradation and different repair conditions is presented and discussed. The first investigation focuses on the effect of conditioning a pristine sample at different dwelling temperatures. The deterioration of bulk laminate properties, such as the glass transition temperature, modulus, and strength, is compared with that of the neat resin samples. Second, the recovery of deteriorated mechanical properties in damaged short-beam samples under the different identified repair parameters is discussed. The third investigation, involving the repair of a fracture surface induced by a different loading mechanism, demonstrates the extensibility and applicability of the results presented in this work.

3.2.1. Effect of isothermal dwellings on laminate properties of short beam samples

To qualify the relationship between results at the resin and laminate scales, oscillating temperature sweeps are performed on the DMA apparatus using short-beam samples pre-exposed to elevated temperatures for 20 min. Similar to the neat resin case, the T_g decreases as indicated in Fig. 4a. Table S4 compares T_g of neat resin samples and short-beam laminates exposed to equivalent isothermal high-temperature dwellings. Within the inspected temperature range, the effect of the dwelling on the reduction of the glass transition temperature is, on average, approximately twice as pronounced as in the neat resin state. This contradictory effect may be justified by higher integral temperatures resulting from improved heat transfer enabled by aligned glass fibers [71], therefore favouring degradation. Further, deterioration of the fiber-matrix interfaces can accelerate the thermal degradation of the resin by providing additional pathways for oxygen diffusion and enhancing the release of volatile degradation products [72]. As a result, the resin in the laminate experiences more extensive degradation than the bulk resin, manifesting in a more pronounced T_g drop.

Five short-beam samples for each preconditioning temperature are loaded to failure, and the recoded apparent stiffness and strength values are reported in Fig. 4b with numerical data provided in Table S5. All the samples exhibit interlaminar shear failure at the central interfaces, manifested as single or multiple delaminations, primarily at the longitudinal-transverse layer interfaces. As this is the expected failure mode for this type of test, the results are considered reliable. A microscopic image of the sample side after loading to failure, resin embedding, and polishing is shown in Fig. 5. In addition to the primary failure mode, transverse cracks can be observed on transverse beads.

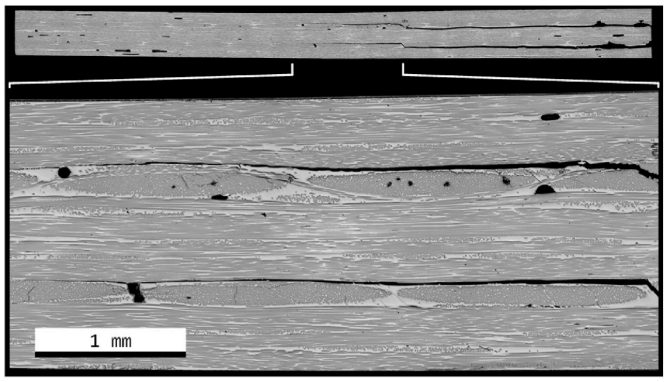

Fig. 5. Example of the observed failure mode within the short beam samples. The micrography is obtained after sample failure and resin embedding. Areas not belonging to the sample have been colored black to improve contrast.

Both stiffness and strength remain relatively constant over a wide temperature range. Although a slight increase in stiffness is observed, it stays within the limits of measurement uncertainty. Only at conditioning temperatures above 240 °C (with computed thermogravimetric degradation of 2.5 %), a significant deterioration of the laminate's apparent mechanical strength and stiffness properties occurs. This decline in strength begins earlier at 230 °C, following a temporary increase in stiffness. The effect of fiber strength degradation on laminate strength is expected to be limited, as the first effect is observed at 250 °C [73]. The samples have been cooled slowly after the conditioning phase, so that thermal stresses are expected to be minimal near the glass transition temperature. A reduction in the glass transition temperature lowers the so-called stress-free temperature and, in turn, the thermal strains and stresses at room temperature by reducing ΔT [74]. These results indicate that while the matrix characterization may be used to support the preselection of healing conditions, it is not sufficient on its own to predict laminate degradation behaviour and thus to optimize healing parameters. On the one hand, the presence of fiber-matrix interfaces accelerates the thermal degradation of the matrix, as evidenced by the accelerated T_g decrease. On the other hand, the presence of fibers mitigates the apparent deterioration in quasistatic modulus and strength, particularly below 230 °C. Still, the high scattering makes it challenging to outline a clear trend in the laminate stiffness and strength. Thus, no direct relationship can be established without further considering the fiber-induced promotion of matrix degradation at appropriate scale. Nevertheless, given the observed trends, the healing parameters established for the neat matrix appear overly optimistic when considering the accelerated degradation in the laminate.

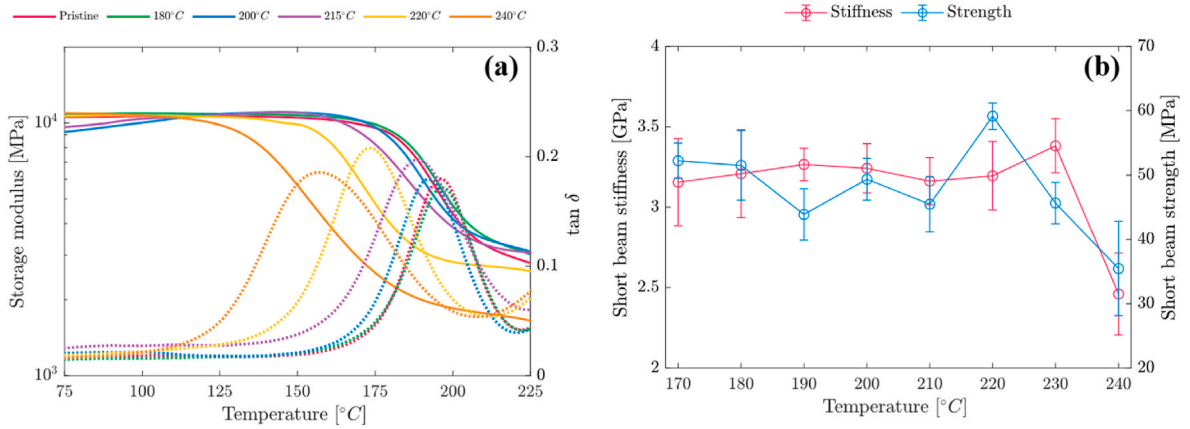

Fig. 4. Effect of 20 min isothermal dwellings at different temperatures with resulting degradation of 0.05 %, 0.15 %, 0.4 %, 0.7 % and 2.5 % on modulus development (a) and the short-beam apparent stiffness and strength (b).

Having extended the investigation of the isolated effects of thermogravimetric degradation on mechanical property deterioration to the laminate level, the laminate behaviour during healing is investigated in the upcoming section for several scenarios (cf. Fig. 3d). With the understanding that degradation will be more pronounced under some selected repair parameter conditions, the results of the repair trials are discussed in the following section.

3.2.2. Repairing capabilities of interlaminar cracks in short beam samples

Two repair approaches are investigated with respect to their experimental feasibility and achievable repair efficiency. As described in the experimental methods section, these procedures involve applying external pressure and vacuum bagging in an oven. For each approach, five short-beam samples are first subjected to failure. Subsequently, the repair condition with index 2 (cf. Table 1) is applied using either vacuum bagging or external consolidation pressure, and the corresponding results are presented in Fig. 6. By comparing the residual stiffness of damaged samples with that of repaired samples, it is clear that using a vacuum alone during repair is insufficient to restore sample integrity. Stiffness is a good indicator of repair capability, as it is mainly determined by interfacial bonding, i.e., matrix adhesion. The hot press-repaired samples, however, exhibit significant stiffness recovery. Also, the selected repair consolidation pressure of 10 MPa appears sufficient to overcome the matrix's high viscosity upon bond exchange, close cracks, and thereby join fractured surfaces. Regardless of the applied pressure, the overall laminate thickness remains unchanged. Consequently, all further repairs are carried out with heated press consolidation at the defined pressure level. This result highlights that a significant pressure application is a prerequisite for successful healing. No further investigation into the influence of this parameter on repair efficiency is conducted.

Results of repairing failed short-beam samples with a hot press, using time-temperature parameters in Table 1 are provided in Fig. 7, with numerical data reported in Table S6 and a representation of the load ramps in Fig. S6. Maximum recovery ratios of 93 % for stiffness and 80 % for strength are achieved, which are very reasonable results compared to other high-performance vitrimers with dynamic disulfide bonds, which range from 60 to 72 % [31,45] for the strength and 89 % [31] for the stiffness. It should also be mentioned that the T_g of the resin investigated in the present study is located approximately 20 °C above the resin systems examined in the literature and that the boundaries for the repairing are, therefore, significantly limited due to the degradation that occurs. Although complete recovery would be expected based on previous estimation of the bond exchange times $\langle \tau_d \rangle$, no full recovery is observed. This discrepancy likely arises from neglecting phenomena such as heat conduction, resin flow, and diffusion phenomena, so that $\langle \tau_d \rangle$ values underestimate the actual repair time.

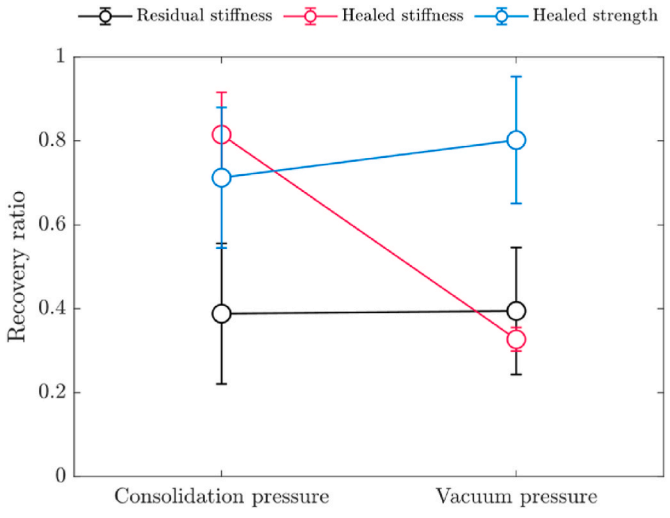

Fig. 6. Effect of pressure on the recovery of short beam stiffness and strength.

Besides that, the strength and stiffness recovery ratios temporarily increase at dwelling temperatures of 215 °C and 225 °C, indicating preferred repair temperatures before a substantial contribution of thermal degradation counteracts the repair process, causing a decline in the recovery ratios.

The specimen failure is assumed to be primarily matrix-driven, as no fiber damage is detectable on the sectioned and polished sample surface. Nonetheless, fiber–matrix debonding cannot be ruled out; therefore, the strength recovery process may not be solely governed by matrix healing.

Increasing the pressurized dwelling time from 10 to 30 min (Fig. 7b) improves the strength recovery, while the modulus recovery shows a slight decrease. It may be argued that, for the short beam samples, the stiffness recovery reflects the extent of the crack surface restoration and the stiffness of these interfaces. In this regard, short-term dwelling is sufficient to close crack interfaces by forming multiple localized junctions, thereby restoring global stiffness. With medium-term dwelling, however, flow-induced dilation of the interfacial defects, caused by the uneven pressure profile, may reduce the effective joint area, leading to a modest drop in stiffness recovery. The scatter along this trend precludes a definitive interpretation of the underlying mechanism. In addition to the mechanisms considered above, vapor-pressure-assisted void growth by the release of gaseous SO_2 [49] could play a role. Resolving this behavior will require further experimentation and interpretation. Over the long term, oxidation and thermal cleavage of the dynamic disulfide moieties accumulate, diminishing modulus recovery. Laminate strength recovery, controlled by the initiation of failure, is more demanding because it requires extensive resin flow to repair the fiber-matrix interface fully. Conversely, short-term dwelling produces only a shallow repair, while medium-term dwelling provides sufficient time for resin flow, promoting more substantial healing and higher-strength recovery. Nevertheless, when dwelling exceeds the optimal window, thermal degradation again becomes significant, reducing the recovered strength.

Similar to high-temperature dwelling and the accompanying thermal degradation of disulfide bonds, long dwell times of 40 min result in reduced strength and stiffness. Therefore, dwelling times of 30 min should not be exceeded, and to recover both strength and strain, dwelling times of 20–30 min are recommended. Although Wool's crack healing theory [75,76] has been previously applied to vitrimers [36,39], the power law relationship of recovery ratio R with time ($R \sim t^{1/2}$) seems not applicable for the vitrimer system investigated in the present study (with T_g being located close to degradation regime). The extended healing times are accompanied by thermal degradation, which counteracts the expected increase in healing efficieny and disrupts the established power-law behavior (cf. Fig. S7), thereby highlighting the increased complexity of these material systems arising from the interplay between healing and degradation.

The intrinsic self-healing of the polymer networks depends on microscopic flow, and molecular interdiffusion, causing chain entanglement [32,77] and dynamic bond-exchange kinetics [77]. With these processes not fully completed, minor interfacial defects with lower chain entanglements and unbonded regions due to fiber-fiber contact remain [78], preventing full recovery of stiffness and strength. Further, it remains unknown whether functional groups on fiber surfaces (epoxy) directly participate in the curing process and whether disulfide moieties immediately located at the fiber surface can undergo dynamic rearrangements during repair. The presence of these defective regions on the fracture surface may explain the reduced stiffness and strength recovery by lowering the bonding area or acting as stress concentrators, as proposed in Ref. [39]. This phenomenon thus depends on the crack morphology and loading mode, so it may be expected that the recovery

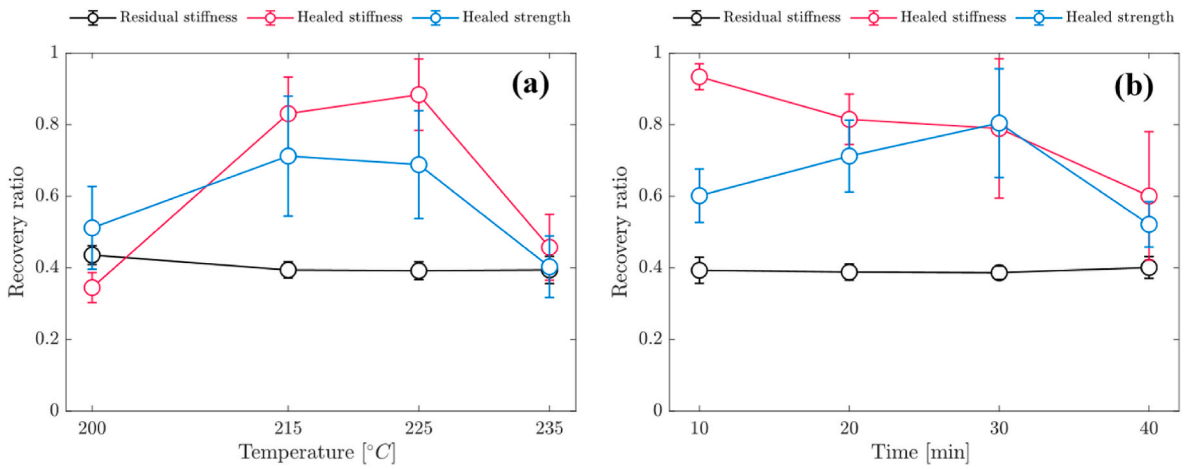

Fig. 7. Effect of temperature for 20 min isothermal dwellings (a) and resistance time at 215 °C (b) on the recovery of short beam stiffness and strength.

ratios in the next section will differ.

The choice of a suitable repairing regime has a decisive influence on the recovery ratio. These experimental findings suggest that the choice of an appropriate repair regime significantly affects repair performance. Even high-performance vitrimers can exhibit outstanding repair performance if the boundary conditions for repair are carefully selected and repair is balanced with degradation. In particular, it is important to note that the relaxation time for bond exchange significantly underestimates the time required for the apparent repair process, as evidenced by the failure to reach full recovery.

3.2.3. Repairing capabilities of interlaminar cracks in double cantilever beam samples

As noted in the previous section, different loading conditions and the resulting cracked surface morphologies are expected to produce different recovery efficiencies. Therefore, two DCB samples are tested under quasistatic conditions with a constant displacement-opening rate at the beam extremities, as described in section 2.2.2. The loading led to the propagation of the crack surface between the two longitudinal fibre-reinforced layers. A small amount of fibre bridging is present at the crack tip during the test, but it is limited as transverse weft fibers hold the unidirectional tows. A picture of the sample during loading is shown in Fig. S8. The samples have been repaired using the heated press with the central processing parameter identified with index 2 in Table 1. After repair, the crack interface exhibited noticeably brittle behaviour during pre-crack opening, as positioning the blade at the same location used for the pristine specimens produced a significantly longer initial crack length, measured at 100 mm from the hinge for both samples. After testing the repaired samples at the same displacement rate as the intact samples, the resulting crack length, crosshead displacement, and force are processed to obtain the fracture energy dissipated during the test. The computed results are shown in Fig. 8, which highlights a significant difference in fracture-propagation resistance between the two cases.

The average recovery ratio for fracture toughness in the crack-propagation regime is calculated to be 10–15 %. This poor result opens the discussion about the repairing capability of different damage modes. While the fracture opening mode and stress scenario differ, the opened interfaces also exhibit different morphologies. In the short-beam samples, the fracture opening occurs between longitudinal and transverse plies, whereas in the DCB tests it occurs between the longitudinal plies only. Upon further inspection of the fracture surface using the micrographic scan shown in Fig. S9, it becomes evident that most of the exposed phase is fibre rather than matrix material, indicating that the matrix could have played a minor role in the healing process. To verify this claim, the fracture surfaces of short-beam samples have been inspected, as shown in Fig. S10. The tested short-beam samples, as

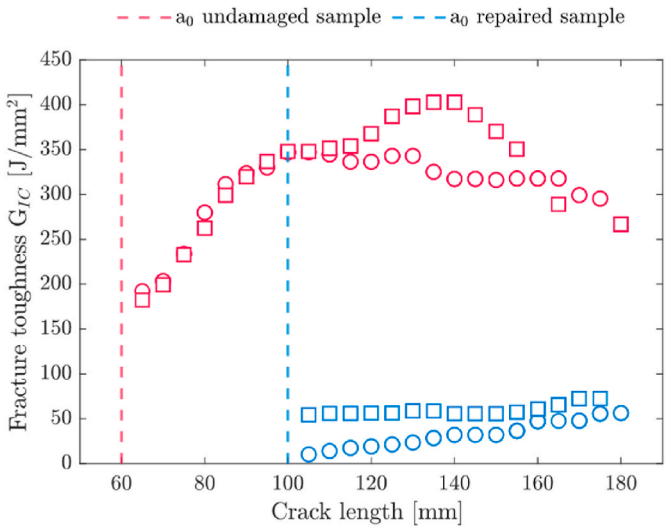

Fig. 8. Fracture toughness G_{IC} as a function of the crack length. Red symbols represent the results for the pristine specimens, while blue markers indicate the energy of repaired samples.

illustrated in Fig. 5, show an open crack interface. The two extremities of the crack have been pulled manually, separating the two parts. Each of these two parts has two crack surfaces: one opened during short-beam testing and the other in a tension-opening mode similar to that in DCB testing (cf. Fig. S10). A distinct difference in surface morphology is observed between these two areas. Respectively, the former displays a smooth resin-rich surface, whereas the latter shows exposed fibres. These results support the observation that the fiber-matrix interphase and the (possibly constrained) molecular rearrangements responsible for healing within it must be considered in the design of a repairable fiber-reinforced material.

3.3. Overall discussion

Ultimately, the present work integrates kinetic degradation modelling, matrix characterization, and laminate experiments to define a suitable repair window for vitrimer-based composites that require extreme temperatures (>200 °C). The kinetic model accurately predicts early-stage thermal degradation and, linking with mechanical and thermomechanical testing, identifies a critical limit of ~0.5 % mass loss, beyond which T_g, crosslink density, and tensile properties deteriorate. Interestingly, the decrease in crosslink density can temporarily increase

bond exchange rates, thereby promoting accelerated healing. However, this effect is offset by the simultaneous deterioration in performance and therefore remains hypothetical.

Overall, the first part presents a transferable framework for estimating the time-temperature regime required for vitrimer reprocessability and healing, explicitly accounting for thermal degradation and its effect on mechanical performance. By balancing healing capabilities and thermal degradation, this integrated approach supports the selection of a suitable time-temperature regime for the repair operation and can guide practical repair design. However, some limitations become evident. The proposed model does not account for mesoscale factors such as heat transfer, resin flow, or interfacial constraints, which ultimately influence laminate repair performance. In other words, the time estimated from matrix stress-relaxation in the rubbery state appears to underestimate the duration of the actual healing process. In addition, we show that the presence of fibers promotes matrix degradation by comparing resin and FRP degradation, and characterizing the matrix alone seems insufficient for a precise estimate of the repair regime, yielding a more optimistic estimate.

Despite these limitations, we show that the framework enables the user to identify a practical repair regime, in this case, 20 min dwelling at 215 °C, balancing sufficiently fast bond exchange with acceptable degradation. Pressure-assisted consolidation proved essential for microstructural restoration, enabling short-beam samples to recover up to 93 % of their stiffness and 80 % of their strength within the prescribed regime. Conversely, derivation from the prescribed regime due to excessively long dwell times and overly high or low temperatures considerably reduces recovery ratios below 50 %. Therefore, laminate tests confirmed the general trends predicted at the resin level, though mechanical responses exhibited greater scatter due to fibre architecture and interface effects.

A significant finding is the apparent dependence of repairability on damage mode. Shear-driven short-beam cracks expose matrix-rich surfaces that can undergo chain interdiffusion and dynamic bond exchange, whereas tensile-driven DCB fractures expose fibre-dominated surfaces with limited polymer available for healing, yielding only 10–15 % fracture-toughness recovery. This demonstrates that the capability of molecular rearrangements within the vitrimer matrix alone does not ensure repairability; crack morphology and the fibre–matrix interphase critically govern the achievable recovery.

4. Conclusion

In conclusion, this study demonstrates the feasibility and limitations of repairing GFRP laminates using a high-performance vitrimer resin and introduces an integrative, systematic framework for designing reliable laminate repair protocols. By explicitly accounting for the narrow processing window, due to the overlap between degradation and dynamic bond exchange regimes, time–temperature processing maps were developed to guide repair cycle design. Even a modest thermogravimetric weight reduction of 2.5 % has been reported to cause substantial deterioration in the mechanical performance of the vitrimer resin (40 % loss in strength, 13 % loss in T_g), underscoring the necessity for precise temperature control during the repair. When repairs were conducted within the prescribed optimized processing window, ex-situ repair exhibited excellent stiffness and strength recovery ratios (93 % and 80 %), whereas deviations from the prescribed conditions resulted in reduced recovery.

The results further reveal that repair efficiency cannot be derived solely from matrix characterisation, and that the underlying damage mode strongly influences repairability. Fiber-dominated facture surfaces clearly require further investigation, as their effective repair likely depends on strategies targeting fibre–matrix interface restoration, such as localized resin delivery. This single-cycle repair assessment clarifies the degradation present after this process and provides a basis for optimizing the multiple-repair durability of vitrimer-based composites. Although multiphysics phenomena, including heat conduction, resin flow, and diffusion, were not explicitly modelled, their influence on the repair effectiveness is clearly indicated and represents an important direction for future studies.

Beyond the specific material system studies, the proposed processing-map-based framework is directly transferable to other vitrimer matrices and composite architectures. It provides a general methodology for defining safe repair windows, quantifying degradation limits, and deriving favourable time-temperature cycles for structural composite repair. As such, the present findings support the development of certifiable repair procedures for vitrimer-based composites, with clear potential for application in aerospace and other structural sectors.

CRediT authorship contribution statement

Niklas Lorenz: Writing – review & editing, Writing – original draft, Visualization, Validation, Methodology, Investigation, Formal analysis, Data curation, Conceptualization. **Mirko Simonetto:** Writing – review & editing, Writing – original draft, Validation, Methodology, Investigation, Formal analysis, Data curation, Conceptualization. **Valea Wisniewsk:** Writing – review & editing, Resources. **Björn Riecken:** Writing – review & editing, Resources. **Baris Kumru:** Writing – review & editing, Investigation, Funding acquisition.

Declaration of generative AI and AI-assisted technologies in the writing process

During the preparation of this work, the authors used Grammarly in order to improve language and readability. After using this tool, the authors reviewed and edited the content as needed and take full responsibility for the content of the publication.

Declaration of competing interest

The authors declare the following financial interests/personal relationships which may be considered as potential competing interests: Niklas Lorenz reports article publishing charges were provided by Delft University of Technology. If there are other authors, they declare that they have no known competing financial interests or personal relationships that could have appeared to influence the work reported in this paper.

Acknowledgments

This project is made possible partly by a contribution from the National Growth Fund program NXTGEN HIGHTECH 01 (NGFNH2201). The authors acknowledge continuous support from the ASM department and technical staff. Specifically, we want to thank Roy Awater, Victor Horbowiec, Dave Ruijtenbeek, Alexander Uithol, and Chantal de Zeeuw for the steadfast assistance through the various experimental procedures.

Appendix A. Supplementary data

Supplementary data to this article can be found online at https://doi.org/10.1016/j.compositesb.2025.113314.

Data availability

The data that support the findings of this study are available from the corresponding author upon reasonable request.

References

[1] Jin F-L, Li X, Park S-J. Synthesis and application of epoxy resins: a review. J Ind Eng Chem 2015;29:1–11. https://doi.org/10.1016/j.jiec.2015.03.026.

[2] Yang Y, Xu Y, Ji Y, Wei Y. Functional epoxy vitrimers and composites. Prog Mater Sci 2021;120:100710. https://doi.org/10.1016/j.pmatsci.2020.100710.

[3] Alabiso W, Schlögl S. The impact of vitrimers on the industry of the future: chemistry, properties and sustainable forward-looking applications. Polymers 2020;12:1660. https://doi.org/10.3390/polym12081660.

[4] Liu Y, Yu Z, Wang B, Li P, Zhu J, Ma S. Closed-loop chemical recycling of thermosetting polymers and their applications: a review. Green Chem 2022;24:5691–708. https://doi.org/10.1039/D2GC00368F.

[5] Wang Y, Cui X, Ge H, Yang Y, Wang Y, Zhang C, et al. Chemical recycling of carbon fiber reinforced epoxy resin composites via selective cleavage of the carbon–nitrogen bond. ACS Sustainable Chem Eng 2015;3:3332–7. https://doi.org/10.1021/acssuschemeng.5b00949.

[6] Oliveux G, Dandy LO, Leeke GA. Current status of recycling of fibre reinforced polymers: review of technologies, reuse and resulting properties. Prog Mater Sci 2015;72:61–99. https://doi.org/10.1016/j.pmatsci.2015.01.004.

[7] Ruiz de Luzuriaga A, Markaide N, Salaberria AM, Azcune I, Rekondo A, Grande HJ. Aero grade epoxy vitrimer towards commercialization. Polymers 2022;14. https://doi.org/10.3390/polym14153180.

[8] Yaghoubi V, Kumru B. Retrosynthetic life cycle assessment: a short perspective on the sustainability of integrating thermoplastics and artificial intelligence into composite systems. Adv Sustain Syst 2024;8:2300543. https://doi.org/10.1002/adsu.202300543.

[9] Lal HM, Uthaman A, Li C, Xian G, Thomas S. Combined effects of cyclic/sustained bending loading and water immersion on the interface shear strength of carbon/glass fiber reinforced polymer hybrid rods for bridge cable. Constr Build Mater 2022;314:125587. https://doi.org/10.1016/j.conbuildmat.2021.125587.

[10] Naebe M, Abolhasani MM, Khayyam H, Amini A, Fox B. Crack damage in polymers and composites: a review. Polym Rev 2016;56:31–69. https://doi.org/10.1080/15583724.2015.1078352.

[11] Lu Z, Jiang M, Pan Y, Xian G, Yang M. Durability of basalt fibers, glass fibers, and their reinforced polymer composites in artificial seawater. Polym Compos 2022;43:1961–73. https://doi.org/10.1002/pc.26511.

[12] Maragoni L, Carraro PA, Simonetto M, Quaresimin M. A novel method to include crack-induced delamination in a fatigue damage predictive procedure for composite laminates. Compos Sci Technol 2023;238:110011. https://doi.org/10.1016/j.compscitech.2023.110011.

[13] Low- and medium-velocity impact as a cause of failure in polymer matrix composites. Failure mechanisms in polymer matrix composites. Woodhead Publishing; 2012. p. 53–78. https://doi.org/10.1533/9780857095329.1.53.

[14] Montarnal D, Capelot M, Tournilhac F, Leibler L. Silica-like malleable materials from permanent organic networks. Science 2011;334:965–8. https://doi.org/10.1126/science.1212648.

[15] Lewis B, Dennis JM, Park C, Shull KR. Glassy dynamics of epoxy-amine thermosets containing dynamic, aromatic disulfides. Macromolecules 2024. https://doi.org/10.1021/acs.macromol.4c01012. acs.macromol.4c01012.

[16] Azcune I, Elorza E, Ruiz De Luzuriaga A, Huegun A, Rekondo A, Grande H-J. Analysis of the effect of network structure and disulfide concentration on vitrimer properties. Polymers 2023;15:4123. https://doi.org/10.3390/polym15204123.

[17] Ruiz de Luzuriaga A, Solera G, Azcarate-Ascasua I, Boucher V, Grande H-J, Rekondo A. Chemical control of the aromatic disulfide exchange kinetics for tailor-made epoxy vitrimers. Polymer 2022;239:124457. https://doi.org/10.1016/j.polymer.2021.124457.

[18] Lorenz N, Dyer WE, Kumru B. High-performance vitrimer entailing renewable plasticizer engineered for processability and reactivity toward composite applications. ACS Appl Polym Mater 2025;7:1934–46. https://doi.org/10.1021/acsapm.4c03731.

[19] Lorenz N, Dyer WE, Kumru B. Exploring the cure state dependence of relaxation and the vitrimer transition phenomena of a disulfide-based epoxy vitrimer. J Polym Sci 2025:1–13. https://doi.org/10.1002/pol.20250463. n/a.

[20] Zhao S, Abu-Omar MM. Recyclable and malleable epoxy thermoset bearing aromatic imine bonds. Macromolecules 2018;51:9816–24. https://doi.org/10.1021/acs.macromol.8b01976.

[21] Li B, Zhu G, Hao Y, Ren T. Effect of cross-link density on the performance of polyimine/epoxy vitrimers. Smart Mater Struct 2024;33:025014. https://doi.org/10.1088/1361-665X/ad1c54.

[22] Lorenz N, Dyer WE, Kumru B. Thermo-rheological and kinetic characterization and modeling of an epoxy vitrimer based on polyimine exchange. Soft Matter 2024;10.1039. https://doi.org/10.1039/D4SM00724G. D4SM00724G.

[23] Amfilochiou V, Debsharma T, De Baere I, Daelemans L, Du Prez F, Van Paepegem W. Thermomechanical characterisation of reprocessable, siloxane-based, glass-fibre-reinforced vitrimers. Compos B Eng 2024;276. https://doi.org/10.1016/j.compositesb.2024.111354.

[24] Debsharma T, Amfilochiou V, Wróblewska AA, De Baere I, Van Paepegem W, Du Prez FE. Fast dynamic siloxane exchange mechanism for reshapable vitrimer composites. J Am Chem Soc 2022;144:12280–9. https://doi.org/10.1021/jacs.2c03518.

[25] Denissen W, Rivero G, Nicolaÿ R, Leibler L, Winne JM, Du Prez FE. Vinylogous urethane vitrimers. Adv Funct Mater 2015;25:2451–7. https://doi.org/10.1002/adfm.201404553.

[26] Krishnakumar B, Sanka RVSP, Binder WH, Parthasarthy V, Rana S, Karak N. Vitrimers: associative dynamic covalent adaptive networks in thermoset polymers. Chem Eng J 2020;385:123820. https://doi.org/10.1016/j.cej.2019.123820.

[27] Schenk V, Labastie K, Destarac M, Olivier P, Guerre M. Vitrimer composites: current status and future challenges. Mater Adv 2022;3:8012–29. https://doi.org/10.1039/D2MA00654E.

[28] Lorenz N, Zawadzki T, Keller L, Fuchs J, Fischer K, Hopmann C. Characterization and modeling of an epoxy vitrimer based on disulfide exchange for wet filament winding applications. Polym Eng Sci 2024. https://doi.org/10.1002/pen.26805.

[29] Memon H, Wei Y, Zhu C. Recyclable and reformable epoxy resins based on dynamic covalent bonds – present, past, and future. Polym Test 2022;105:107420. https://doi.org/10.1016/j.polymertesting.2021.107420.

[30] van der Zwaag S, Grande AM, Post W, Garcia SJ, Bor TC. Review of current strategies to induce self-healing behaviour in fibre reinforced polymer based composites. Mater Sci Technol 2014;30:1633–41. https://doi.org/10.1179/1743284714Y.0000000624.

[31] Benazzo F, Rigamonti D, Bettini P, Sala G, Grande AM. Interlaminar fracture of structural fibre/epoxy composites integrating damage sensing and healing. Compos B Eng 2022;244:110137. https://doi.org/10.1016/j.compositesb.2022.110137.

[32] Garcia SJ. Effect of polymer architecture on the intrinsic self-healing character of polymers. Eur Polym J 2014;53:118–25. https://doi.org/10.1016/j.eurpolymj.2014.01.026.

[33] Kamble M, Vashisth A, Yang H, Pranompont S, Picu CR, Wang D, et al. Reversing fatigue in carbon-fiber reinforced vitrimer composites. Carbon 2022;187:108–14. https://doi.org/10.1016/j.carbon.2021.10.078.

[34] Barnett PR, Brackenridge JA, Advincula AA, Taussig LA, Nepal D. Reformable and sustainable thermosetting carbon fiber composites from epoxy vitrimer. Compos B Eng 2024;274:111270. https://doi.org/10.1016/j.compositesb.2024.111270.

[35] Arano FM, Casado U, Ferrero IZ, Rivera J, Churruca MJ, Altuna FI, et al. Self-healing of microcracks and scratches in a carbon-fiber reinforced epoxy vitrimer by conventional or remote heating. ACS Appl Mater Interfaces 2025;17:13170–8. https://doi.org/10.1021/acsami.4c18025.

[36] Perrin H, Vaudemont R, Del Frari D, Verge P, Puchot L, Bodaghi M. On the cyclic delamination-healing capacity of vitrimer-based composite laminates. Compos Appl Sci Manuf 2024;177:107899. https://doi.org/10.1016/j.compositesa.2023.107899.

[37] Mandal T, Ozten U, Vaught L, Meyer JL, Amiri A, Polycarpou A, et al. Processing and mechanics of aromatic vitrimeric composites at elevated temperatures and healing performance. J Compos Sci 2024;8:252. https://doi.org/10.3390/jcs8070252.

[38] El Arwadi O, Raut A, Meyer JL, Polycarpou A, Naraghi M. Time and temperature-dependent fracture mechanics of self-healing vitrimers. Polymer 2025;322:128148. https://doi.org/10.1016/j.polymer.2025.128148.

[39] Hayder R, Kedziora S. Cyclic healing of delamination in amine-epoxy vitrimer carbon fiber composites. Results Eng 2025;28:107405. https://doi.org/10.1016/j.rineng.2025.107405.

[40] Amfilochiou V, Debsharma T, De Baere I, Du Prez F, Van Paepegem W. Interlaminar fracture toughness behaviour of a repairable glass-fibre-reinforced vitrimer for wind-energy applications. Compos B Eng 2025;291:112023. https://doi.org/10.1016/j.compositesb.2024.112023.

[41] Lopez-Olmedo A, Frassine R, Longana ML. Towards repairable composites: healing of mode I and mode II delaminations in woven glass fibre and vitrimer matrix laminates. Compos B Eng 2025;305:112738. https://doi.org/10.1016/j.compositesb.2025.112738.

[42] Schenk V, Olivier P, Labastie K, Destarac M, Guerre M. Carbon fibres/RTM6 vitrimer and non-dynamic epoxy thermoset composites: comparative study of manufacturing, mechanical characteristics, water absorption, impact resistance, repairing and compression after impact. Compos B Eng 2025;304:112674. https://doi.org/10.1016/j.compositesb.2025.112674.

[43] Glass transition temperature testing of composites 2024. https://www.compositesworld.com/articles/glass-transition-temperature-testing-of-composites. [Accessed 31 October 2024].

[44] Schenk V, D'Elia R, Olivier P, Labastie K, Destarac M, Guerre M. Exploring the limits of high-T(g) epoxy vitrimers produced through resin-transfer molding. ACS Appl Mater Interfaces 2023;15:46357–67. https://doi.org/10.1021/acsami.3c10007.

[45] Kosarli M, Foteinidis G, Tsirka K, Markaide N, Ruiz de Luzuriaga A, Calderón Zapatería D, et al. 3R composites: knockdown effect assessment and repair efficiency via mechanical and NDE testing. Appl Sci 2022;12:7269. https://doi.org/10.3390/app12147269.

[46] Aranberri I, Landa M, Elorza E, Salaberria AM, Rekondo A. Thermoformable and recyclable CFRP pultruded profile manufactured from an epoxy vitrimer. Polym Test 2021;93:106931. https://doi.org/10.1016/j.polymertesting.2020.106931.

[47] Alms J, Sambale AK, Fuchs J, Lorenz N, von den Berg N, Conen T, et al. Qualification of the vitrimeric matrices in industrial-scale wet filament winding processes for Type-4 pressure vessels. Polymers 2025;17:1146. https://doi.org/10.3390/polym17091146.

[48] Schenk V, De Calbiac J, D'Elia R, Olivier P, Labastie K, Destarac M, et al. Epoxy vitrimer formulation for resin transfer molding: reactivity, process, and material characterization. ACS Appl Polym Mater 2024;6:6087–95. https://doi.org/10.1021/acsapm.4c00796.

[49] Sanchez-Rodriguez D, Zaidi S, Jahani Y, Ruiz De Luzuriaga A, Rekondo A, Maimi P, et al. Processability and reprocessability maps for vitrimers considering thermal degradation and thermal gradients. Polym Degrad Stabil 2023;217:110543. https://doi.org/10.1016/j.polymdegradstab.2023.110543.

[50] ASTM International. ASTM D2344/D2344M – 22, standard test method for short-beam strength of polymer matrix composite materials and their laminates. 2022.

[51] ASTM International. ASTM D5528/D5528M – 21, standard test method for mode I interlaminar fracture toughness of unidirectional fiber-reinforced polymer matrix composites. 2022.

[52] Sanchez-Rodriguez D, Zaidi S, Jahani Y, Ruiz De Luzuriaga A, Rekondo A, Maimi P, et al. Processability and reprocessability maps for vitrimers considering thermal degradation and thermal gradients. Polym Degrad Stabil 2023;217:110543. https://doi.org/10.1016/j.polymdegradstab.2023.110543.
[53] Sanchez-Rodriguez D, Zaidi S, Carreras L, Ruiz de Luzuriaga A, Rekondo A, Costa J, et al. Time-temperature-transformation diagrams from isoconversional kinetic analyses applied to the processing and reprocessing of vitrimers. Thermochim Acta 2024;736:179744. https://doi.org/10.1016/j.tca.2024.179744.
[54] Das P, Tiwari P. Thermal degradation kinetics of plastics and model selection. Thermochim Acta 2017;654:191–202. https://doi.org/10.1016/j.tca.2017.06.001.
[55] Sbirrazzuoli N. Determination of pre-exponential factors and of the mathematical functions f(α) or G(α) that describe the reaction mechanism in a model-free way. Thermochim Acta 2013;564:59–69. https://doi.org/10.1016/j.tca.2013.04.015.
[56] Tziamtzi CK, Chrissafis K. Optimization of a commercial epoxy curing cycle via DSC data kinetics modelling and TTT plot construction. Polymer 2021;230. https://doi.org/10.1016/j.polymer.2021.124091.
[57] Vyazovkin S. Isoconversional kinetics of thermally stimulated processes. 2015.
[58] Vyazovkin S, Burnham AK, Criado JM, Pérez-Maqueda LA, Popescu C, Sbirrazzuoli N. ICTAC kinetics committee recommendations for performing kinetic computations on thermal analysis data. Thermochim Acta 2011;520:1–19. https://doi.org/10.1016/j.tca.2011.03.034.
[59] Friedman HL. Kinetics of thermal degradation of char-forming plastics from thermogravimetry. Application to a phenolic plastic. J Polym Sci Part C: Polymer Symposia 1964;6:183–95. https://doi.org/10.1002/polc.5070060121.
[60] Farjas J, Roura P. Isoconversional analysis of solid-state transformations: a critical review. Part III. Isothermal and non isothermal predictions. J Therm Anal Calorim 2012;109:183–91. https://doi.org/10.1007/s10973-011-1642-2.
[61] Williams G, Watts DC. Non-symmetrical dielectric relaxation behaviour arising from a simple empirical decay function. Trans Faraday Soc 1970;66:80–5. https://doi.org/10.1039/TF9706600080.
[62] Riggleman RA, Lee H-N, Ediger MD, Pablo JJ de. Heterogeneous dynamics during deformation of a polymer glass. Soft Matter 2010;6:287–91. https://doi.org/10.1039/B912288E.
[63] Wang T, Chen Y, Chen B, Suazo MJ, Purwanto NS, Torkelson JM. Reprocessable, self-healing, and creep-resistant covalent adaptable network made from chain-growth monomers with dynamic covalent thionourethane and disulfide cross-links. ACS Macro Lett 2024;13:1147–55. https://doi.org/10.1021/acsmacrolett.4c00391.
[64] Jewell B, Sain T. From network degradation to mechanical brittleness: the aging response of epoxy vitrimers. Polym Degrad Stabil 2025;242:111654. https://doi.org/10.1016/j.polymdegradstab.2025.111654.
[65] Jewell B, Abadi PP, Sain T. Experimental characterization and constitutive modeling of bulk epoxy under thermo-oxidative aging. Polym Degrad Stabil 2025;234:111215. https://doi.org/10.1016/j.polymdegradstab.2025.111215.
[66] Fanlo P, Konuray O, Ochoteco O, Ximenis M, Rekondo A, Jürgen Grande H, et al. Dynamic by design: unlocking full relaxation in disulfide epoxy networks. Polym Chem 2025;16:2701–17. https://doi.org/10.1039/D5PY00124B.
[67] Gerritzen J, Muller-Pabel M, Muller J, Groger B, Lorenz N, Hopmann C, et al. Development of a high-fidelity framework to describe the process-dependent viscoelasticity of a fast-curing epoxy matrix resin including testing, modelling, calibration and validation. Polymers 2022;14. https://doi.org/10.3390/polym14173647.
[68] Marks MJ, Snelgrove RV. Effect of conversion on the structure-property relationships of amine-cured epoxy thermosets. ACS Appl Mater Interfaces 2009;1:921–6. https://doi.org/10.1021/am900030u.
[69] White SR, Mather PT, Smith MJ. Characterization of the cure-state of DGEBA-DDS epoxy using ultrasonic, dynamic mechanical, and thermal probes. Polym Eng Sci 2002;42:51–67. https://doi.org/10.1002/pen.10927.
[70] Olivier L, Ho NQ, Grandidier JC, Lafarie-Frenot MC. Characterization by ultra-micro indentation of an oxidized epoxy polymer: correlation with the predictions of a kinetic model of oxidation. Polym Degrad Stabil 2008;93:489–97. https://doi.org/10.1016/j.polymdegradstab.2007.11.012.
[71] Takizawa Y, Chung DDL. Through-thickness thermal conduction in glass fiber polymer–matrix composites and its enhancement by composite modification. J Mater Sci 2016;51:3463–80. https://doi.org/10.1007/s10853-015-9665-x.
[72] Demleitner M, Endner L, Ruckdäschel H. Lifetime prediction of thermo-oxidative degradation of a modified epoxy resin and its glass fiber composite in air atmosphere and correlation with long-term aging behavior. Polym Degrad Stabil 2025;242:111686. https://doi.org/10.1016/j.polymdegradstab.2025.111686.
[73] Feih S, Manatpon K, Mathys Z, Gibson AG, Mouritz AP. Strength degradation of glass fibers at high temperatures. J Mater Sci 2009;44:392–400. https://doi.org/10.1007/s10853-008-3140-x.
[74] Lorenz N, Fischer K, Hopmann C. Surface waviness of continuous fiber-reinforced polymer composites – a review on their formation, characterization and modeling. Compos Appl Sci Manuf 2025;198:109067. https://doi.org/10.1016/j.compositesa.2025.109067.
[75] Wool RP, O'Connor KM. Time dependence of crack healing. J Polym Sci, Polym Lett Ed 1982;20:7–16. https://doi.org/10.1002/pol.1982.130200102.
[76] Wool RP. Adhesion at polymer–polymer interfaces: a rigidity percolation approach. C R Chim 2006;9:25–44. https://doi.org/10.1016/j.crci.2005.04.008.
[77] Li B, Cao P-F, Saito T, Sokolov AP. Intrinsically self-healing polymers: from mechanistic insight to current challenges. Chem Rev 2023;123:701–35. https://doi.org/10.1021/acs.chemrev.2c00575.
[78] Khan T, Irfan MS, Cantwell WJ, Umer R. Crack healing in infusible thermoplastic composite laminates. Compos Appl Sci Manuf 2022;156:106896. https://doi.org/10.1016/j.compositesa.2022.106896.